

L^3 : Scene-agnostic Visual Localization in the Wild

Yu Zhang  Muhua Zhu  Yifei Xue  Tie Ji  Yizhen Lao* 

Hunan University, Changsha, Hunan 410082, China

{yuzhang, casmyzhu, iflyhsueh, yizhenlao}@hnu.edu.cn, jietie_hnu@163.com

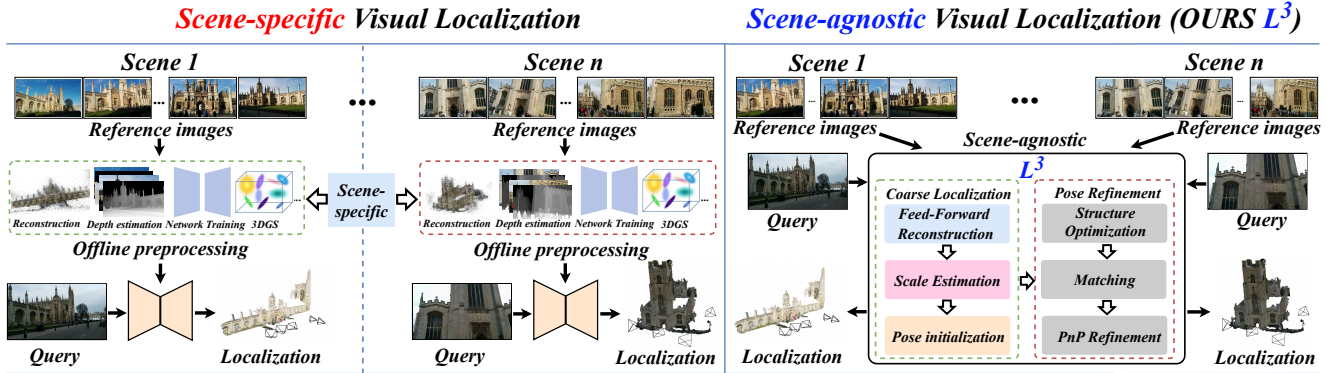


Figure 1. **Comparison between scene-specific and scene-agnostic visual localization paradigms.** *Scene-specific* methods require extensive offline preprocessing such as reconstruction or per-scene network training. In contrast, our proposed *scene-agnostic* visual localization framework L^3 directly estimates query poses via feed-forward coarse localization and PnP refinement, generalizing to novel scenes without requiring scene representations or preprocessing.

Abstract

Standard visual localization methods typically require offline pre-processing of scenes to obtain 3D structural information for better performance. This inevitably introduces additional computational and time costs, as well as the overhead of storing scene representations. Can we visually localize in a wild scene **without** any off-line preprocessing step? In this paper, we leverage the online inference capabilities of feed-forward 3D reconstruction networks to propose a novel map-free visual localization framework L^3 . Specifically, by performing direct online 3D reconstruction on RGB images, followed by two-stage metric scale recovery and pose refinement based on 2D-3D correspondences, L^3 achieves high accuracy without the need to pre-build or store any offline scene representations. Extensive experiments demonstrate L^3 not only that the performance is comparable to state-of-the-art solutions on various benchmarks, but also that it exhibits significantly superior robustness in sparse scenes (fewer reference images per scene).

*Corresponding author

1. Introduction

Visual localization, a fundamental task in robotics, autonomous driving, and virtual reality, aims to estimate the 6-DoF pose of a query image from a set of database images with known poses.

Existing visual localization solutions are mainly categorized into structure-based approaches and image-based approaches: **1)** Structure-based methods typically store a 3D geometric representation of the scene (3D maps), such as point clouds [34, 36, 40], meshes [33], NeRF [13, 32, 49–51], 3DGS [28], or the weights of scene coordinate regression networks [4, 7, 18, 39, 43]. By establishing 2D-3D correspondences between the query image and the 3D map, the camera pose can be estimated using the Perspective-n-Point (PnP) solver. **2)** In contrast, image-based methods represent the scene as a database of images with poses instead of 3D maps. These approaches rely on image retrieval for the pose approximation [1–3, 20] or on directly regressing the absolute pose through neural architectures [12, 14, 21, 25, 38]. In addition, [19] proposed to enhance image databases with local depth maps, enabling the establishment of 2D-3D cor-

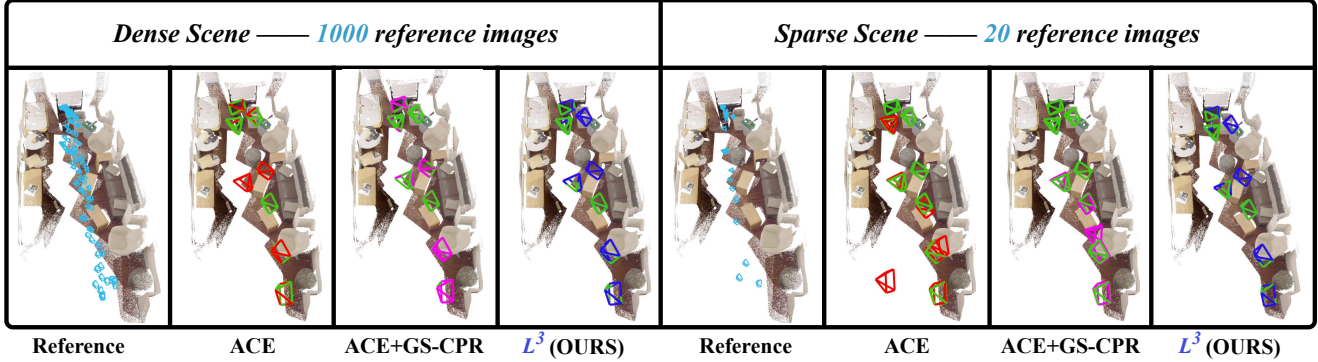


Figure 2. **Comparison of dense and sparse scenes.** Green denotes ground truth query poses and references are cyan. The predicted poses by different methods are shown in different colors: red for ACE [7], magenta for ACE+GS-CPR [28], and blue for our proposed L^3 . **Dense Scene:** Localization using all 1000 reference images. **Sparse Scene:** We sampled the 1000 reference images and retain only 20. Our L^3 significantly outperforms other baselines in this challenging case.

respondences for PnP without explicitly reconstructing a global 3D structure.

However, structure-based methods generally achieve superior accuracy but require reconstructing and storing a 3D map of the scene before querying. Image-based methods circumvent explicit 3D reconstruction but also require network training (APR) or depth map prediction (depth-map augmentation) before the query phase. **In summary**, existing visual localization approaches generally mandate **scene-specific** offline preprocessings, which are usually time-consuming and computationally expensive. Given this, we raise a core question: *Does robust visual localization necessarily require scene-specific priors, such as pre-built maps or optimized networks?*

To address these challenges, we propose L^3 , a paradigm-shifting framework for scene-agnostic visual localization, as shown in Fig. 1. Building upon the inference capabilities of the feed-forward 3D reconstruction network π^3 [46], our framework jointly processes a query image and a set of retrieved reference images to perform direct online reconstruction. By leveraging the strong generalization power of the model, L^3 generates high-quality camera poses and dense geometry in a single pass, completely **bypassing any scene-specific offline training or pre-built 3D maps**. However, the resulting initial poses and point clouds inherently lack a consistent metric scale. To resolve this, we propose a two-stage scale recovery strategy that combines local geometric consistency with global trajectory constraints. Following scale restoration, we perform structure-only bundle adjustment (BA) to optimize the 3D point clouds, fixing the ground-truth poses of the reference cameras. Finally, the refined 6-DoF pose of the query image is recovered through guided matching and a PnP solver between the query image and the optimized 3D structure.

In contrast to existing methods that rely on extensive pre-

processing, L^3 achieves high localization accuracy while entirely eliminating the necessity for scene-specific offline training or pre-built 3D maps. Furthermore, as demonstrated in Fig. 2, our approach not only delivers competitive performance in dense scenarios but also exhibits remarkable robustness under challenging sparse conditions. Consequently, the only required offline processing is the retrieval of reference images, facilitating **instant deployment in uncharted environments**. Our codes will public online. Our contributions are summarized as follows:

- We propose L^3 , a scene-agnostic framework for visual localization. To the best of our knowledge, it is the first to achieve performance comparable to state-of-the-art (SOTA) methods without any offline scene-specific optimization or pre-3D-mapping.
- We design a novel coarse-to-fine localization pipeline featuring a two-stage scale recovery strategy and a structure-only BA which enables accurate metric scale restoration.
- Extensive evaluations on multiple indoor and outdoor benchmarks demonstrate that L^3 generalizes effectively across diverse environments. It not only excels in standard dense-view settings but also exhibits superior robustness in sparse-view scenarios, significantly outperforming existing methods under extreme data constraints.

2. Related Work

Structure-based methods. Conventional structure-based methods [34–36] rely on feature matching and 3D point clouds reconstructed via Structure from Motion (SfM) to derive 2D-3D correspondences for pose estimation, yet they face unavoidable storage overhead despite techniques like point cloud sparsification [8, 48] or descriptor compression [16, 22]. Scene Coordinate Regression (SCR) avoids explicit maps by training scene-specific networks to directly regress 3D coordinates, evolving from early

random forests [9, 10, 39] to differentiable architectures like DSAC* [4, 5] and efficient decoupled models like ACE [7]. Recent SCR extensions such as GLACE [43] and R-SCoRe [18] further enhance robustness in large-scale environments through feature diffusion or covisibility constraints. Alternatively, novel view synthesis (NVS) follows a render-and-compare paradigm, where NeRF-based approaches optimize photometric loss [24, 49], integrate radiance fields into Monte Carlo filters [29], or power data augmentation [31] and pose refinement [13]. Latest works leverage internal radiance representations for feature-level matching [50, 51]. Concurrently, 3D Gaussian Splatting (3DGS) has been utilized for one-shot pose estimation [30]. Furthermore, frameworks like GS-CPR [28] leverage 3DGS alongside foundation models such as MAST3R [23] to establish robust correspondences.

Image-based methods. Image-based methods handle dynamic scene changes without explicit 3D structures [1–3, 20], typically utilizing image retrieval to approximate poses for subsequent initialization. Absolute Pose Regression (APR) [11, 12, 14, 21, 38] maps images directly to 6-DoF poses in a single pass, yet remains limited by lower accuracy and the requirement for scene-specific training [27, 37]. To bridge accuracy and flexibility, ImLoc [19] constructs 2D-3D correspondences via depth-map augmentation instead of global models, though it still necessitates triangulation-based depth estimation for all reference images prior to querying.

Feed-forward 3D Reconstruction. Feed-forward models like Dust3R [45] and MAST3R [23] enable direct camera pose estimation and scene reconstruction from image sequences, though they often encounter high global alignment costs and stability issues at scale. To mitigate these constraints, Fast3R [47] introduces multi-view parallel processing to handle large-scale inputs, while VGGT [44] and π^3 [46] leverage multi-task pre-training on massive datasets to achieve SOTA accuracy and robustness. In particular, π^3 provides a permutation-invariant framework with affine-invariant pose predictions.

3. Methodology

Problem Statement. Given a query image $I_q \in \mathbb{R}^{H \times W \times 3}$ with camera intrinsics $\mathbf{K}_q \in \mathbb{R}^{3 \times 3}$, we assume that the top- K candidate reference images $\{I_{r,i}\}_{i=1}^K$ have been retrieved. Our goal is to estimate the absolute 6-DoF query pose $\mathbf{P}_q = [\mathbf{R}_q | \mathbf{t}_q] \in SE(3)$ by leveraging the reference images $\{I_{r,i}\}_{i=1}^K$, their corresponding poses $\mathbf{P}_{r,i} = [\mathbf{R}_{r,i} | \mathbf{t}_{r,i}]$ and their intrinsics $\mathbf{K}_{r,i}$. We use $(\cdot)^{GT}$ to denote ground truth, and $(\cdot)^{local}$ for network predictions in the local coordinate system. The subscripts $(\cdot)_r$ and $(\cdot)_q$ indicate reference and query images, respectively.

Framework. As illustrated in Fig. 3, we introduce L^3 , a scene-agnostic framework that estimates absolute camera

poses using only retrieved reference images and their associated camera parameters. The process begins in Sec. 3.1 with a coarse localization module that jointly processes the query and reference images via a 3D feed-forward reconstruction network to produce initial poses and dense geometric predictions. To resolve the scale ambiguity inherent in these feed-forward outputs, we implement a robust two-stage metric scale estimation strategy and utilize the estimated scale to compute the initial global pose of the query image. Finally, in Sec. 3.2, the scale-corrected 3D structure is optimized through structure-only refinement, followed by a PnP solver to determine the final 6-DoF query pose.

3.1. Coarse Localization

Feed-Forward 3D Reconstruction. In this stage, we employ π^3 [46] as the backbone for initial pose estimation, as it is permutation-equivariant and does not enforce the first frame as the origin of the coordinate system. Given a query image $I_q \in \mathbb{R}^{H \times W \times 3}$ and a set of retrieved reference images $\{I_{r,i}\}_{i=1}^K$, the network jointly processes these inputs to generate dense geometry predictions. Formally, let Φ_{π^3} denote the network function and $[\cdot]$ denote the concatenation along the sequence dimension. The feed-forward process is defined as:

$$\mathcal{P}^{local}, \mathbf{P}^{local}, \mathcal{C} = \Phi_{\pi^3} ([I_q, I_{r,1}, \dots, I_{r,K}]) \quad (1)$$

The output includes dense local point clouds $\mathcal{P}^{local} \in \mathbb{R}^{B \times H \times W \times 3}$ and a set of camera poses $\mathbf{P}^{local} \in SE(3)$ for both the query and reference images in a canonical coordinate system, where $B = K + 1$. In addition, for all input images, the network predicts confidence score maps $\mathcal{C}^{B \times H \times W}$ to measure the uncertainty of the prediction at each pixel. We select the reference image with the highest total confidence score as the anchor $I_{r,anc}$ for the subsequent stage.

Scale Estimation. Since the network predictions lack an absolute scale S , we propose a two-stage scale estimation strategy that prioritizes local geometric consistency while enforcing global trajectory constraints as shown in Fig. 4.

- **Stage 1: Local Geometric Consistency.** We leverage the ground truth poses of retrieved reference images to estimate scale via triangulation. For geometric stability, we first sample image pairs $\{(I_{r,i}, I_{r,j})\}$ with a camera baseline empirically constrained within $[0.3, 10]$ meters. For each valid pair, we extract and match keypoints using SuperPoint [15] and LightGlue [26]. These correspondences are then triangulated using the ground truth reference poses to yield a set of 3D points \mathcal{P}^{GT} . Subsequently, each triangulated 3D point $p_n \in \mathcal{P}^{GT}$ associated with the image pair $(I_{r,i}, I_{r,j})$ is projected into the coordinate system of camera i to obtain its absolute depth $Z_{n,i}^{GT}$. Since the network predicts pixel-wise 3D coordinates in the local frame, we can extract the corresponding local depth $Z_{n,i}^{local}$ by indexing the predicted

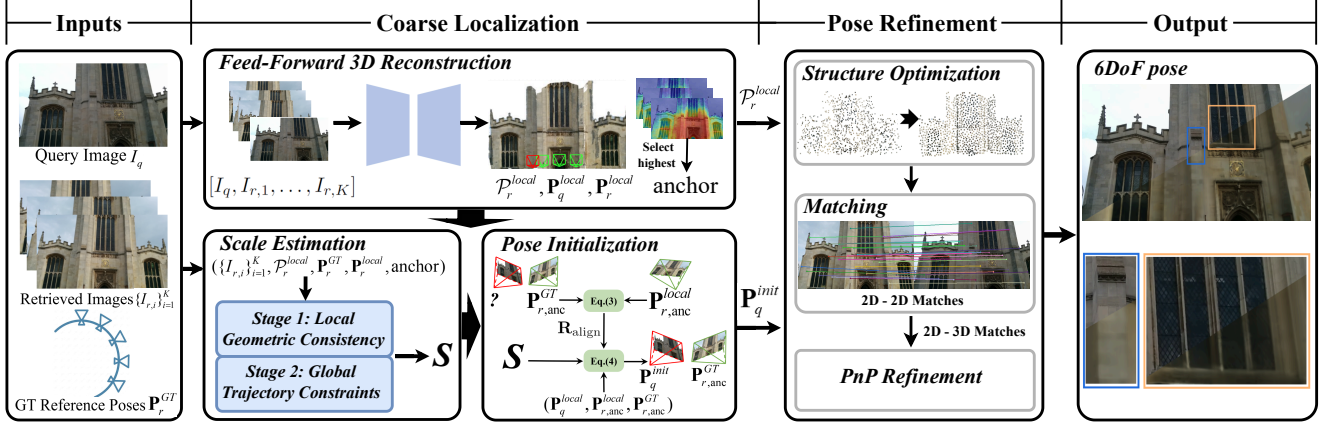


Figure 3. **Overview of L^3 .** **Coarse Localization:** Given a query image I_q and retrieved references $\{I_{r,i}\}_{i=1}^K$, we first perform feed-forward 3D reconstruction to predict local point clouds \mathcal{P}_r^{local} , query pose \mathbf{P}_q^{local} and reference poses \mathbf{P}_r^{local} . A scale estimation module then computes the scale factor S via a two-stage strategy to initialize the pose \mathbf{P}_q^{init} . **Pose Refinement:** The pose is refined via structure optimization and PnP to yield the final 6-DoF pose \mathbf{P}_q . **Output:** We compare the query image (top-left) with its rendering under the predicted pose (bottom-right), separated by a diagonal line.

local point cloud $\mathcal{P}_{r,i}^{local}$ of camera i at the exact 2D pixel location of p_n . The final metric scale factor S_{tri} is determined by taking the median of the ratios between the absolute and local depths.

• **Stage 2: Global Trajectory Constraints.** To prevent scale estimation failures in sparse views, we introduce a global consistency check. We formally define the trajectory radius r as the root mean square distance from the K reference camera centers $\{\mathbf{C}_i\}_{i=1}^K$ to their centroid $\bar{\mathbf{C}}$. To evaluate an estimated scale S , the relative deviation d between the scaled local radius r^{local} and the ground truth radius r^{GT} is computed as:

$$r = \sqrt{\frac{1}{K} \sum_{i=1}^K \|\mathbf{C}_i - \bar{\mathbf{C}}\|_2^2}, \quad d = \left| \frac{S \cdot r^{local}}{r^{GT}} - 1 \right| \quad (2)$$

Applying the triangulated scale S_{tri} to the predicted reference poses yields an initial deviation d_{tri} . If d_{tri} falls below a 5% threshold, we adopt S_{tri} as the final scale. Otherwise, we proceed to Stage 2, where we compute an alignment rotation matrix \mathbf{R}_{align} using the anchor image $I_{r,anc}$, leveraging the scale-invariance of rotational transformations. Using its predicted rotation $\mathbf{R}_{r,anc}^{local}$ from $\mathbf{P}_{r,anc}^{local}$ and ground truth rotation $\mathbf{R}_{r,anc}^{GT}$ from $\mathbf{P}_{r,anc}^{GT}$, \mathbf{R}_{align} is computed as:

$$\mathbf{R}_{align} = \mathbf{R}_{r,anc}^{GT} (\mathbf{R}_{r,anc}^{local})^\top \quad (3)$$

Applying this matrix \mathbf{R}_{align} aligns the orientation of the local coordinate system with the global coordinate system. After rotation alignment, we estimate the scale within a RANSAC [17] framework. At each iteration, we randomly sample a pair of cameras and compute a candidate scale as the ratio of their ground truth Euclidean distance to the

predicted distance. By applying this scale to the entire trajectory, we then compute the offset between the centroids of the predicted and ground truth trajectories as the global translation. We define cameras with a pose alignment error of ≤ 10 cm as inliers. After 500 iterations, the scale that maximizes the number of inliers is selected as S_{traj} . We then compare its corresponding trajectory deviation d_{traj} against d_{tri} , ultimately adopting the scale associated with the smaller deviation.

Pose initialization. Since all image poses are predicted in the local coordinate system, we compute the relative pose from the query to the anchor image. Utilizing the estimated metric scale S , the alignment rotation matrix \mathbf{R}_{align} , and the anchor’s ground truth pose $\mathbf{P}_{r,anc}^{GT} = [\mathbf{R}_{r,anc}^{GT} | \mathbf{t}_{r,anc}^{GT}]$, the initial global pose of the query image $\mathbf{P}_q^{init} = [\mathbf{R}_q^{init} | \mathbf{t}_q^{init}]$ is derived as follows:

$$\begin{aligned} \mathbf{R}_q^{init} &= \mathbf{R}_{align} \mathbf{R}_q^{local}, \\ \mathbf{t}_q^{init} &= \mathbf{t}_{r,anc}^{GT} + \mathbf{R}_{align} (S \cdot (\mathbf{t}_q^{local} - \mathbf{t}_{r,anc}^{local})) \end{aligned} \quad (4)$$

3.2. Pose Refinement

With the predicted point cloud $\mathcal{P}_{r,i}^{local}$ and initial pose \mathbf{P}_q^{init} , we proceed to refine the pose. This process involves the following steps:

Structure Optimization. Unlike traditional SfM which relies on triangulation for initialization, we fully leverage the dense geometry provided by the network. This enables the efficient and stable acquisition of 3D structures, even under sparse view configurations. To ensure high-quality 2D-3D correspondences, we re-select the anchor image specifically for this optimization stage. We designate the first reference image as the new anchor due to its highest feature similarity with the query image, as validated in the supplementary ma-

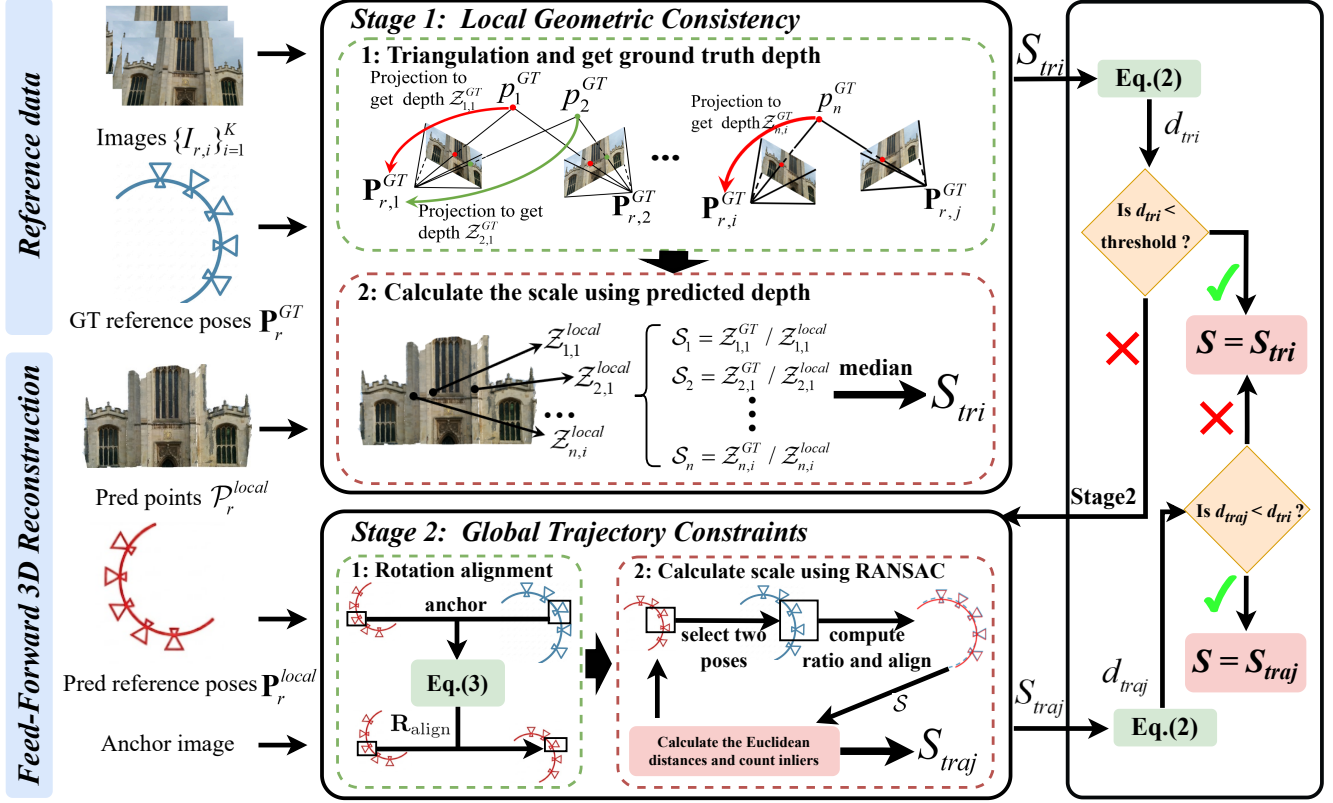


Figure 4. **Scale Estimation Strategy.** **Stage 1:** Absolute depths are triangulated using ground truth (GT) reference poses. If the median ratio S_{tri} between GT and local depths (from \mathcal{P}_r^{local}) has a deviation d_{tri} below a threshold, S_{tri} is adopted. **Stage 2:** Otherwise, we align the **predicted trajectory** \mathcal{P}_r^{local} with the **GT trajectory** \mathcal{P}_r^{GT} via rotation R_{align} . A RANSAC scheme then yields the scale S_{traj} by minimizing Euclidean distance error. S_{traj} is accepted if $d_{traj} < d_{tri}$ (fallback to S_{tri} otherwise).

terial. We then construct global feature tracks by merging pairwise matches between this anchor and the other reference images. For each track, we initialize its 3D coordinates \mathbf{X}_k by back-projecting the anchor’s 2D keypoint using its corresponding scaled network-predicted depth. We then perform a structure-only Bundle Adjustment. By fixing the ground truth reference poses $\{\mathbf{P}_{r,i}^{GT}\}$ and refining only the 3D coordinates \mathbf{X}_k , we minimize the multi-view projection error:

$$\arg \min_{\{\mathbf{X}_k\}} \sum_k \sum_{i \in \mathcal{O}_k} \rho(\|\pi(\mathbf{P}_{r,i}^{GT}, \mathbf{X}_k) - \mathbf{u}_{k,i}\|^2) \quad (5)$$

where $\pi(\cdot)$ is the projection function, \mathcal{O}_k denotes the set of view indices (including the anchor) observing the k -th point, $\mathbf{u}_{k,i}$ is the observed 2D keypoint of track k in view i , and $\rho(\cdot)$ is the Soft $L1$ loss function.

Matching. We project the optimized 3D points $\{\mathbf{X}_k\}$ onto the query image:

$$\hat{\mathbf{u}}_k = \pi(\mathbf{P}_q^{init}, \mathbf{X}_k) \quad (6)$$

For each projected point $\hat{\mathbf{u}}_k$, we define a local search region (set to a 20-pixel radius in our experiments) and retrieve

candidate keypoints extracted from the query image. We compute the descriptor distance between the reference descriptors associated with the 3D points and the candidate query descriptors. Matches are established using a nearest neighbor search within the local region, effectively filtering out outliers and reducing search complexity.

PnP Refinement. The guided matching process yields a set of 2D-3D correspondences $\mathcal{M} = \{(\mathbf{u}_{q,k}, \mathbf{X}_k)\}$. We estimate the final 6-DoF query pose \mathbf{P}_q by solving the PnP problem. Taking the coarse pose \mathbf{P}_q^{init} as the initialization, we apply RANSAC [17] and then refine the pose on the inlier set by using the Levenberg-Marquardt algorithm:

$$\mathbf{P}_q^* = \arg \min_{\mathbf{P}} \sum_{(\mathbf{u}, \mathbf{X}) \in \mathcal{M}} \|\pi(\mathbf{P}, \mathbf{X}) - \mathbf{u}\|^2 \quad (7)$$

To ensure maximum robustness, we evaluate both the refined pose \mathbf{P}_q^* and the initial pose \mathbf{P}_q^{init} based on their inlier counts with respect to the query image. The pose yielding the larger inlier count is ultimately selected as the final result.

Table 1. **Results on 7Scenes dataset.** We compare the median translation and rotation errors (cm/°) of different methods, lower is better. Best results are in **bold**.

	Methods	Chess	Fire	Heads	Office	Pumpkin	Redkitchen	Stairs	Avg. ↓[cm/°]
APR	PoseNet [21] ¹	10/4.02	27/10.0	18/13.0	17/5.97	19/4.67	22/5.91	35/10.5	21/7.74
	DFNet [12] ¹	3/1.12	6/2.30	4/2.29	6/1.54	7/1.92	7/1.74	12/2.63	6/1.93
	Marepo [14] ²	1.9/0.83	2.3/0.92	2.1/1.24	2.9/0.93	2.5/0.88	2.9/0.98	5.9/1.48	2.9/1.04
SCR	DSAC* [4] ²	0.5/0.17	0.8/0.28	0.5/0.34	1.2/0.34	1.2/0.28	0.7/0.21	2.7/0.78	1.1/0.34
	ACE [7]	0.5/0.19	0.8/0.33	0.5/0.33	1.1/0.29	1.1/ 0.22	0.8/0.20	2.9/0.80	1.1/0.34
	GLACE [43]	0.6/0.18	0.9/0.34	0.6/0.35	1.0/0.29	0.9/0.23	0.8/0.20	3.1/0.95	1.1/0.36
NVS	pNeRFLoc [50]	2/0.8	2/0.88	1/0.83	3/1.05	6/1.51	5/1.54	32/5.73	7.3/1.76
	DFNet + NeFeS ₅₀ [13]	2/0.57	2/0.74	2/1.28	2/0.56	2/0.55	2/0.57	5/1.28	2.4/0.79
	HR-APR [27]	2/0.55	2/0.75	2/1.45	2/0.64	2/0.62	2/0.67	5/1.30	2.4/0.85
	NeRFMatch [51]	0.9/0.3	1.1/0.4	1.5/1.0	3.0/0.8	2.2/0.6	1.0/0.3	10.1/1.7	2.8/0.7
	MCLoc [41]	2/0.8	3/1.4	3/1.3	4/1.3	5/1.6	6/1.6	6/2.0	4.1/1.43
	ACE + GS-CPR [28]	0.5/0.15	0.6/0.25	0.4/0.28	0.9/0.26	1.0/0.23	0.7/0.17	1.4/0.42	0.8/0.25
	L^3 (ours)	0.6/0.21	1.2/0.46	0.7/0.41	1.1/0.32	1.4/0.34	1.0/0.26	3.1/0.87	1.3/0.41

Table 2. **Results on 12Scenes dataset.** We compare the median translation and rotation errors (cm/°) of different methods, and the average accuracy of frames under a specified threshold. Best results are in **bold**.

	Methods	Avg. ↓[cm/°]	Avg. ↑[5cm, 5°]	Avg. ↑[1cm, 1°]
APR	Marepo [14] ²	2.1/1.04	95	—
SCR	ACE [7]	0.7/0.26	100	75.1
	GLACE [43]	0.7/0.25	100	78.7
NVS	ACE + GS-CPR [28]	0.5/0.21	100	86.7
	L^3 (ours)	0.4/0.19	99.5	86.7

4. Experiments

• **Datasets.** We evaluate L^3 on three benchmarks: the indoor *7Scenes* [39] and *12Scenes* [42] datasets, utilizing SfM ground truth from [6], and the outdoor *Cambridge Landmarks* [21]. While the indoor sets provide varied architectural scales, the outdoor scenes introduce challenging dynamic objects and lighting variations to assess robustness “in the wild”.

• **Metrics.** We assess performance using median *translation* (cm) and *rotation* (°) errors w.r.t camera pose, alongside the *recall rate* to measure the percentage of successful localized rate within specified error thresholds.

• **Setup.** Reference images are retrieved via MegaLoc [2] and filtered with a 0.3m minimum physical baseline to ensure spatial diversity. By default, $K = 10$ reference images are selected per query. All experiments were conducted on an NVIDIA H20 GPU.

• **Baselines.** We compare L^3 against representative image-

based APR methods, including PoseNet [21], DFNet [12], and Marepo [14]. Structure-based baselines encompass SCR networks (DSAC* [4], ACE [7], GLACE [43]) and recent NVS approaches, including NeRF-based variants [13, 27, 50, 51], the representation-agnostic MCLoc [41], and the 3DGS-based GS-CPR [28] (initialized with ACE). For outdoor evaluation on Cambridge Landmarks, we further include feature matching-based Active Search [36], HLoc [34], and ImLoc [19].

4.1. Dense View Localization

We first evaluate L^3 under dense-view configurations, utilizing the complete set of reference images in each dataset.

• **Indoor Localization.** Evaluation results on the 7Scenes dataset are summarized in Tab. 1. Without requiring scene-specific training or reconstruction, L^3 significantly outperforms APR methods (e.g., DFNet, Marepo) and NeRF-based synthesis approaches (e.g., pNeRFLoc, NeRF-Match), while remaining competitive with leading SCR networks like ACE and GLACE. On the more extensive 12Scenes dataset (Tab. 2), L^3 establishes a new SOTA,

¹These data are cited from NeFeS [13].

²These data are cited from GS-CPR [28].

surpassing established SCR frameworks—including ACE and GLACE—as well as the recent NVS-based GS-CPR. These results underscore the efficacy of our scene-agnostic paradigm, which matches or exceeds the precision of structure-based methods without the burden of offline pre-processing.

- **Outdoor Localization.** As reported in Tab. 3, L^3 delivers performance competitive with leading FM pipelines like HLoc and ImLoc while significantly outperforming other baselines. Notably, despite the vastly increased scene scale, L^3 requires no hyperparameter tuning or dataset-specific modifications, underscoring its superior generalization over existing scene-specific solutions.

4.2. Sparse Scene Localization

To evaluate performance under data scarcity, reference image sets are uniformly downsampled into sparse subsets. Accounting for variations in scene scale, we retain $N \in [5, 30]$ images per scene for indoor datasets (7Scenes and 12Scenes) and $N \in [30, 60]$ for the outdoor Cambridge Landmarks. In the extreme $N = 5$ indoor configuration, each query is restricted to retrieving only these five available reference images. We visualize the estimated trajectories and localization errors across different methods under dense and sparse conditions in Fig. 7. As depicted, our method exhibits superior stability compared to baselines.

As illustrated in Fig. 5, L^3 exhibits superior robustness by maintaining the lowest and most stable error growth curves across all benchmarks as sparsity increases. Quantitative results in Tab. 4 reveal that ACE is highly sensitive to data scarcity, often diverging in sparse settings. While GS-CPR performs well on 7Scenes with $N \geq 20$, it fails when reference images are insufficient to support 3DGS training, such as on 12Scenes or the extreme $N = 5$ subset. In contrast, L^3 establishes SOTA performance across all 12Scenes configurations and remains the only framework to maintain stable localization at $N = 5$ on both indoor datasets. On Cambridge Landmarks (Tab. 5), where ACE and GS-CPR accuracy drops sharply, L^3 consistently delivers high precision. Notably, our performance at $N = 30$ is comparable to ACE’s results in the fully dense setting and outpaces GS-CPR by more than an order of magnitude.

4.3. Ablation Study

We ablate scale estimation strategy and pose refinement one by one to quantitatively verify the effectiveness of these two vital modules in L^3 .

- **Analysis of Scale Estimation Strategy.** As illustrated in Fig. 6, our two scale recovery components exhibit distinct complementarity across varying data densities. While local geometric triangulation provides superior precision in dense scenarios, it suffers from unreliable results in sparse settings ($N \leq 10$) due to the

scarcity of effective matches. Conversely, RANSAC-based global trajectory alignment—though less precise in dense scenes—effectively leverages the reconstruction network’s inherent robustness to avoid the drastic error spikes typical of triangulation under data scarcity. By synergizing these strengths, our complete two-stage strategy achieves optimal overall performance and ensures sustained robustness against fluctuations in data density.

- **Effectiveness of Pose Refinement.** We define L^3_{coarse} as the direct network output without the refinement stage, and $L^3_{\text{w/o. Optim}}$ as the output of PnP using network predictions without the structure optimization stage. As evidenced in Tab. 4 and Tab. 5, the pose refinement module significantly enhances localization accuracy across nearly all indoor and outdoor benchmarks. Furthermore, utilizing optimized 3D points for PnP further reduces the localization error. Notably, in sparse scenarios, while L^3_{coarse} inherently demonstrates superior stability compared to existing methods, the refinement module further consistently minimizes localization errors. Crucially, in extremely sparse settings (e.g., $N = 10$ in 12Scenes) where limited optimization points may yield unreliable PnP solutions, our module employs a query-image inlier constraint to retain the initial prediction selectively. This robust fallback mechanism effectively averts the performance degradation observed in methods like GS-CPR.

5. Discussion

- **What are the advantages of L^3 compared to previous methods?** L^3 establishes a “zero-mapping” paradigm for visual localization, achieving high accuracy without any scene-specific offline training or reconstruction. By leveraging the generalization of feed-forward networks such as π^3 [46], our framework performs direct online inference, eliminating the hours of SfM or training required by traditional structure-based methods. This scene-agnostic approach proves exceptionally robust in sparse-view settings where baselines such as ACE [7] and GS-CPR [28] often diverge. Our evaluations verify that the two-stage scale estimation strategy maintains metric consistency under data scarcity, while the query-image inlier check in our refinement module provides a vital fallback to prevent performance degradation. Ultimately, L^3 enables rapid, reliable deployment in uncharted environments with minimal reference data.

- **What are the limitations of L^3 ?** Despite its robust performance, L^3 is subject to several limitations. As shown in Tab. 6, the primary bottleneck is inference latency, which averages 2.1 seconds per query. Additionally, high computational demands limit direct deployment on resource-constrained edge hardware.

- **Potential Applications.** By eliminating the prohibitive preprocessing and storage costs of traditional mapping, L^3

Table 3. **Results on Cambridge Landmarks dataset.** We compare the median translation and rotation errors (cm/°) of different methods. Best results are in **bold**.

Methods		Kings	Hospital	Shop	Church	Avg. ↓[cm/°]
FM	AS (SIFT) [36]	13/ 0.2	20/0.4	4/0.2	8/0.3	11/0.28
	HLoc (SP+SG) [15, 35]	12/ 0.2	15/ 0.3	4/0.2	7/0.2	10/0.23
	ImLoc [19]	11/0.2	14/0.3	4/0.2	7/0.2	9/0.23
APR	LENS [31]	33/0.5	44/0.9	27/1.6	53/1.6	39/1.15
	DFNet [12]	73/2.37	200/2.98	67/2.21	137/4.03	119/2.90
	PMNet [25]	68/1.97	103/1.31	58/2.10	133/3.73	90/2.27
SCR	DSAC* [4]	15/0.3	21/0.4	5/0.3	13/0.4	14/0.35
	ACE [7]	28/0.37	32/0.63	5/0.28	19/0.60	21/0.47
	GLACE [43]	18/0.32	19/0.42	5/0.22	9/0.29	13/0.31
NVS	CrossFire [32]	47/0.7	43/0.7	20/1.2	39/1.4	37/1
	DFNet + NeFeS ₅₀ [13]	37/0.54	52/0.88	15/0.53	37/1.14	35/0.77
	HR-APR [27]	36/0.58	53/0.89	13/0.51	38/1.16	35/0.78
	MCLoc [41]	31/0.42	39/0.73	12/0.45	26/0.88	27/0.62
	ACE + GS-CPR [28]	20/0.29	21/0.40	5/0.24	13/0.40	15/0.33
L^3 (ours)		13/0.22	15/0.30	5/0.23	9/0.31	11/0.27

Table 4. **Sparse view localization on the 7Scenes and 12Scenes datasets.** We report the mean of median translation and rotation errors (cm/°) across all subscenes. N is the number of sampled reference images. “-” indicates localization failure in at least one subscene. Best results are in **bold**.

Datasets	Methods	Dense	Sparse			
			N=30	N=20	N=10	N=5
7Scenes	ACE [7]	1.1/0.34	2.7/0.65	3.2/0.79	9.2/1.53	348.7/4.78
	ACE + GS-CPR [28]	0.8/0.25	1.5/0.42	1.6/0.46	5.2/1.33	-
	L^3_{coarse} (ours)	2.5/0.71	3.7/1.02	4.3/1.17	5.7/1.52	6.4/1.65
	$L^3_{\text{w/o. Optim}}$ (ours)	2.5/0.67	2.8/0.79	3.1/0.84	5.1/1.42	6.5/1.66
	L^3 (ours)	1.3/0.41	1.9/0.56	2.3/0.63	4.5/1.26	5.9/1.61
12Scenes	ACE [7]	0.7/0.26	12.5/1.32	51.3/3.76	837.9/12.1	2950/20.63
	ACE + GS-CPR [28]	0.5/0.21	21.3/0.95	-	-	-
	L^3_{coarse} (ours)	1.0/0.36	2.6/0.90	3.5/1.12	10.8/2.52	16.9/2.56
	$L^3_{\text{w/o. Optim}}$ (ours)	0.7/0.25	1.6/0.54	2.8/0.94	10.7/2.53	17.2/2.57
	L^3 (ours)	0.4/0.19	1.4/0.53	2.7/0.93	10.2/2.51	16.9/2.56

enables instant, scalable localization in uncharted environments using only sparse reference data. While current latency limits real-time edge execution, this scene-agnostic paradigm is ideal for latency-tolerant or distributed architectures. Promising applications include HD mapping for autonomous driving, cloud-edge pose initialization for VR/AR, and the immediate deployment of robotics in unknown terrains.

6. Conclusion

We present L^3 , a paradigm-shifting framework that validates the feasibility of replacing intensive offline preprocessing with direct online 3D reconstruction for visual localization. By leveraging feed-forward dense predictions alongside a robust two-stage scale recovery and pose refinement pipeline, L^3 achieves accuracy competitive with SO-

Table 5. **Results of sparse view localization on the Cambridge dataset.** We compare the mean of the median translation and rotation errors (cm/°) for different methods across all subscenes. Best results are in **bold**.

Methods	Dense	Sparse			
		N=60	N=50	N=40	N=30
ACE [7]	21/0.47	83/1.70	122/2.85	111/2.43	261/5.65
ACE + GS-CPR [28]	15/0.33	41/1.10	72/2.13	88/5.41	350/8.63
L^3 coarse (ours)	36/0.54	42/0.64	40/0.64	56/0.68	54/0.76
L^3 w/o. Optim (ours)	15/0.33	23/0.46	20/0.53	23/0.47	34/0.66
L^3 (ours)	11/0.27	18/0.39	17/0.37	20/0.42	25/0.53

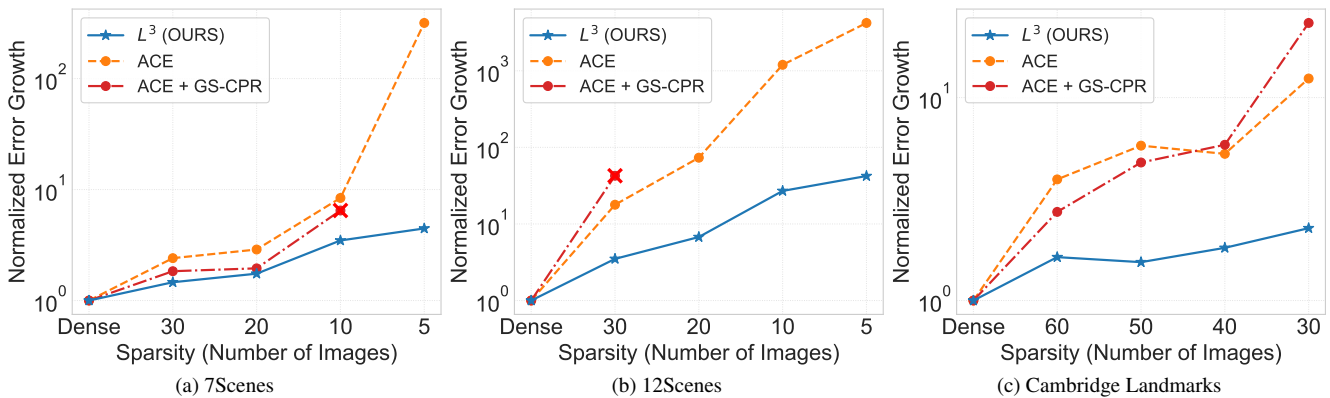


Figure 5. **Robustness analysis under increasing sparsity.** We plot the log-scale translation error growth relative to the dense setting on three datasets. "X" indicates localization failure beyond that sparsity level.

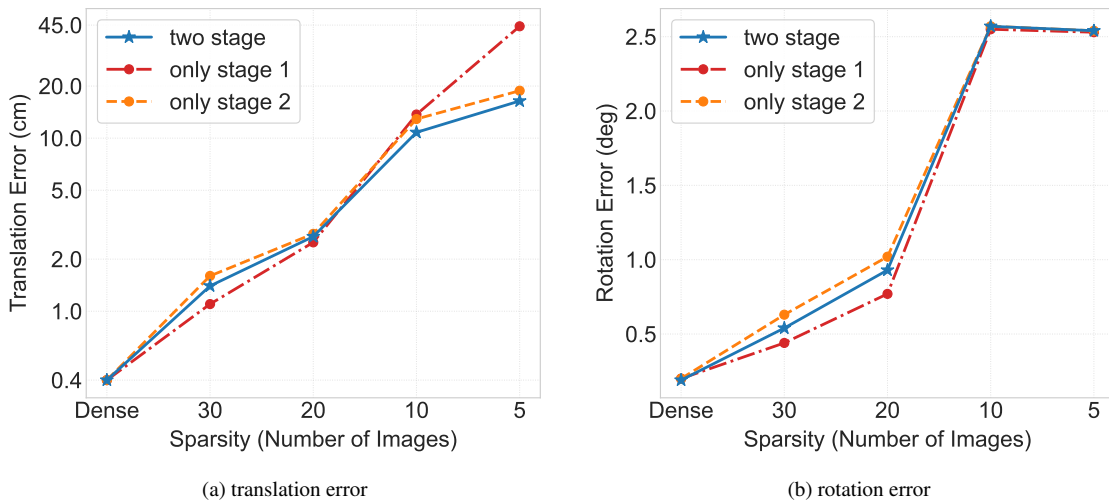
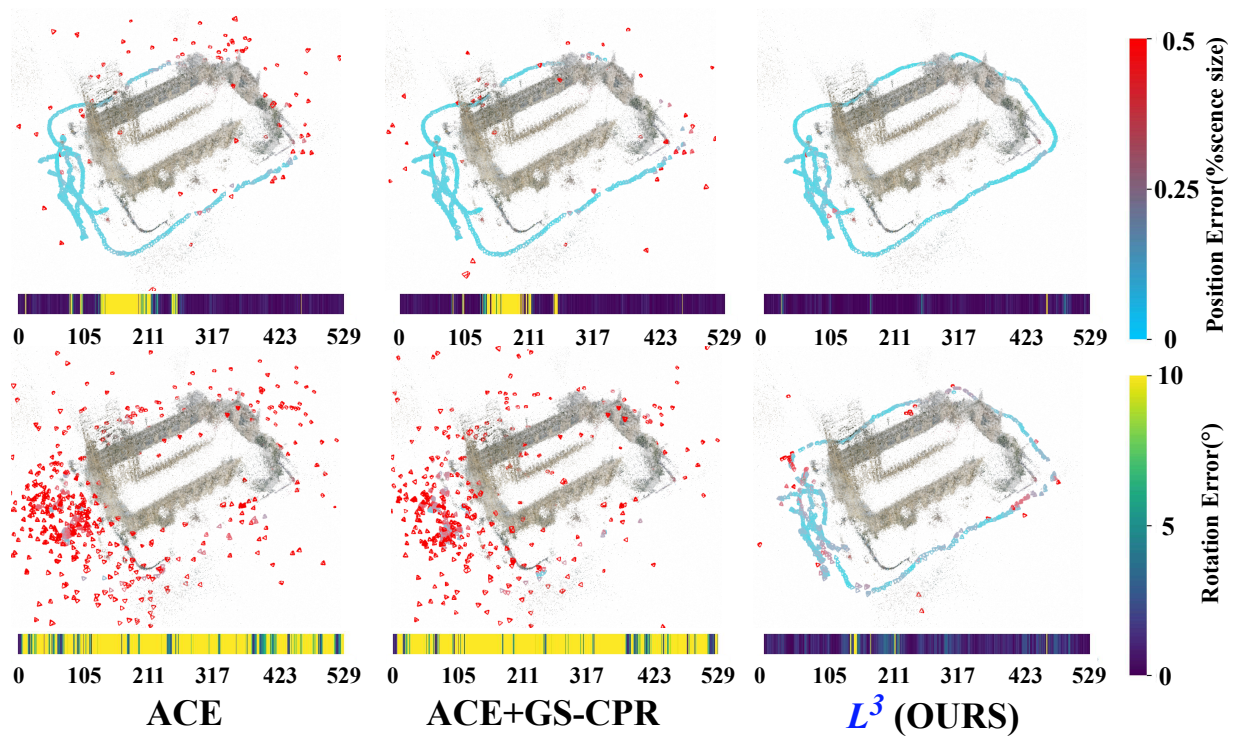


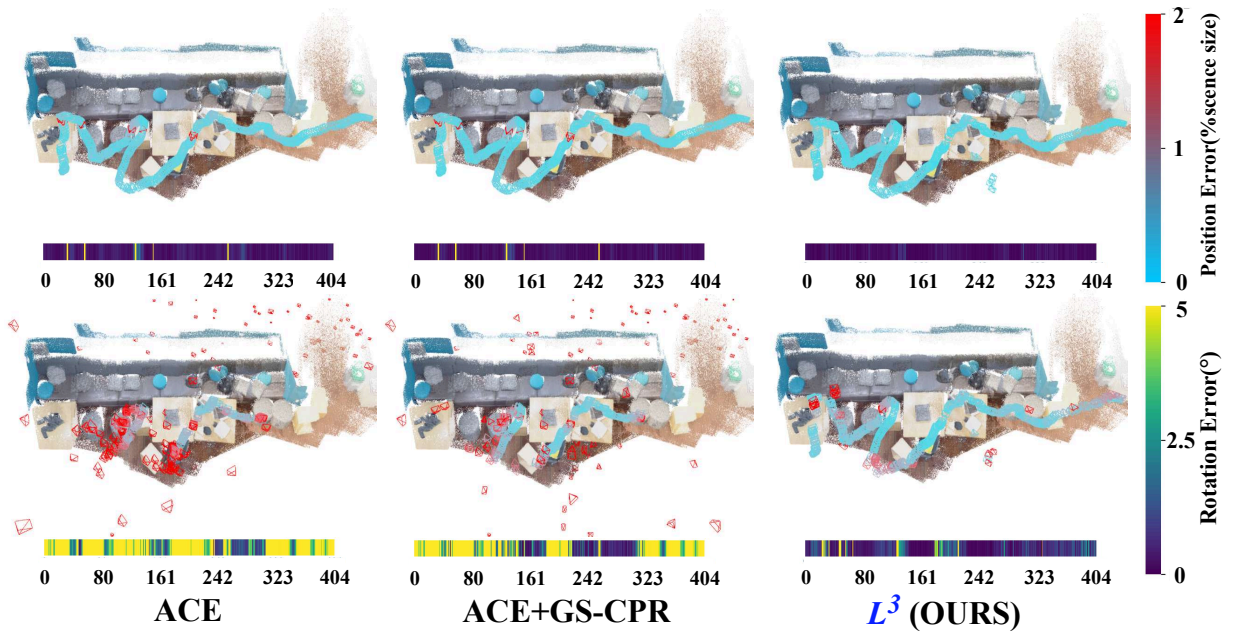
Figure 6. **Ablation of scale estimation strategies on 12Scenes dataset.** We compare our full method in Sec. 3.1 (**blue line**) against variants using only stage 1 (local geometric consistency, **red line**) or stage 2 (global trajectory constraints, **yellow line**).

TAs without the need for pre-built maps or scene-specific optimization. Crucially, our approach exhibits exceptional

robustness in sparse-view scenarios, significantly outperforming existing solutions under extreme data constraints.



(a) StMarysChurch



(b) Office2_5b

Figure 7. **Comparison of localization errors.** Position (trajectories) and rotation (bottom bars, x-axis denotes frame indices) errors are colored by magnitude for ACE [7], GS-CPR [28], and our L^3 . (a) **Outdoor StMarysChurch** (Cambridge Landmarks). (b) **Indoor Office2_5b** (12Scenes). Both panels compare **dense (top)** and **sparse (bottom, $N = 30$)** settings.

This work establishes a new 'zero-mapping' benchmark, facilitating rapid and reliable deployment in unconstrained environments while drastically reducing the storage and

computational overhead for practical engineering applications.

Table 6. **Time comparison on the Cambridge Landmarks dataset.** We only need top retrieval. Best results are in **bold**.

Metrics	ACE [7]	GS-CPR [28]	L^3 (ours)
Pre-processing time (min) ↓	2	31	0.6
Inference time (s) ↓	0.02	0.26	2.1
Storage (MB) ↓	4	203	0
Avg. Error [cm/°] ↓	21/0.47	15/0.33	11/0.27

References

- [1] Relja Arandjelovic, Petr Gronat, Akihiko Torii, Tomas Padilla, and Josef Sivic. Netvlad: Cnn architecture for weakly supervised place recognition. In *CVPR*, pages 5297–5307, 2016.
- [2] Gabriele Berton and Carlo Masone. Megaloc: One retrieval to place them all. In *CVPR*, pages 2861–2867, 2025.
- [3] Gabriele Berton, Gabriele Trivigno, Barbara Caputo, and Carlo Masone. Eigenplaces: Training viewpoint robust models for visual place recognition. In *ICCV*, pages 11080–11090, 2023.
- [4] Eric Brachmann and Carsten Rother. Visual camera re-localization from rgb and rgb-d images using dsac. *IEEE TPAMI*, 44(9):5847–5865, 2021.
- [5] Eric Brachmann, Alexander Krull, Sebastian Nowozin, Jamie Shotton, Frank Michel, Stefan Gumhold, and Carsten Rother. Dsac-differentiable ransac for camera localization. In *CVPR*, pages 6684–6692, 2017.
- [6] Eric Brachmann, Martin Humenberger, Carsten Rother, and Torsten Sattler. On the limits of pseudo ground truth in visual camera re-localisation. In *ICCV*, pages 6218–6228, 2021.
- [7] Eric Brachmann, Tommaso Cavallari, and Victor Adrian Prisacariu. Accelerated coordinate encoding: Learning to relocalize in minutes using rgb and poses. In *CVPR*, pages 5044–5053, 2023.
- [8] Federico Camposeco, Andrea Cohen, Marc Pollefeys, and Torsten Sattler. Hybrid scene compression for visual localization. In *CVPR*, pages 7653–7662, 2019.
- [9] Tommaso Cavallari, Stuart Golodetz, Nicholas A Lord, Julien Valentin, Luigi Di Stefano, and Philip HS Torr. On-the-fly adaptation of regression forests for online camera re-localisation. In *CVPR*, pages 4457–4466, 2017.
- [10] Tommaso Cavallari, Stuart Golodetz, Nicholas A Lord, Julien Valentin, Victor A Prisacariu, Luigi Di Stefano, and Philip HS Torr. Real-time rgb-d camera pose estimation in novel scenes using a relocalisation cascade. *IEEE TPAMI*, 42(10):2465–2477, 2019.
- [11] Shuai Chen, Zirui Wang, and Victor Prisacariu. Direct-posenet: Absolute pose regression with photometric consistency. In *2021 International Conference on 3D Vision (3DV)*, pages 1175–1185, 2021.
- [12] Shuai Chen, Xinghui Li, Zirui Wang, and Victor A Prisacariu. Dfnet: Enhance absolute pose regression with direct feature matching. In *ECCV*, pages 1–17. Springer, 2022.
- [13] Shuai Chen, Yash Bhalgat, Xinghui Li, Jia-Wang Bian, Kejie Li, Zirui Wang, and Victor Adrian Prisacariu. Neural refinement for absolute pose regression with feature synthesis. In *CVPR*, pages 20987–20996, 2024.
- [14] Shuai Chen, Tommaso Cavallari, Victor Adrian Prisacariu, and Eric Brachmann. Map-relative pose regression for visual re-localization. In *CVPR*, pages 20665–20674, 2024.
- [15] Daniel DeTone, Tomasz Malisiewicz, and Andrew Rabinovich. Superpoint: Self-supervised interest point detection and description. In *Proceedings of the IEEE conference on computer vision and pattern recognition workshops*, pages 224–236, 2018.
- [16] Hao Dong, Xieyuanli Chen, Mihai Dusmanu, Viktor Larsson, Marc Pollefeys, and Cyrill Stachniss. Learning-based dimensionality reduction for computing compact and effective local feature descriptors. In *2023 IEEE International Conference on Robotics and Automation, ICRA 2023*, pages 6189–6195. IEEE-Institute of Electrical and Electronics Engineers Inc., 2023.
- [17] Martin A Fischler and Robert C Bolles. Random sample consensus: a paradigm for model fitting with applications to image analysis and automated cartography. *Communications of the ACM*, 24(6):381–395, 1981.
- [18] Xudong Jiang, Fangjinhua Wang, Silvano Galliani, Christoph Vogel, and Marc Pollefeys. R-score: Revisiting scene coordinate regression for robust large-scale visual localization. In *CVPR*, pages 11536–11546, 2025.
- [19] Xudong Jiang, Fangjinhua Wang, Silvano Galliani, Christoph Vogel, and Marc Pollefeys. Imloc: Revisiting visual localization with image-based representation. *arXiv preprint arXiv:2601.04185*, 2026.
- [20] Nikhil Keetha, Avneesh Mishra, Jay Karhade, Krishna Murthy Jatavallabhula, Sebastian Scherer, Madhava Krishna, and Sourav Garg. Anyloc: Towards universal visual place recognition. *IEEE Robotics and Automation Letters*, 9(2):1286–1293, 2023.
- [21] Alex Kendall, Matthew Grimes, and Roberto Cipolla. Posenet: A convolutional network for real-time 6-dof camera relocalization. In *ICCV*, pages 2938–2946, 2015.
- [22] Zakaria Laskar, Iaroslav Melekhov, Assia Benbihi, Shuzhe Wang, and Juho Kannala. Differentiable product quantization for memory efficient camera relocalization. In *ECCV*, pages 470–489. Springer, 2024.
- [23] Vincent Leroy, Yohann Cabon, and Jérôme Revaud. Grounding image matching in 3d with mast3r. In *ECCV*, pages 71–91. Springer, 2024.
- [24] Chen-Hsuan Lin, Wei-Chiu Ma, Antonio Torralba, and Simon Lucey. Barf: Bundle-adjusting neural radiance fields. In *ICCV*, pages 5741–5751, 2021.
- [25] Jingyu Lin, Jiaqi Gu, Bojian Wu, Lubin Fan, Renjie Chen, Ligang Liu, and Jieping Ye. Learning neural volumetric pose features for camera localization. In *ECCV*, pages 198–214. Springer, 2024.
- [26] Philipp Lindenberger, Paul-Edouard Sarlin, and Marc Pollefeys. Lightglue: Local feature matching at light speed. In *ICCV*, pages 17627–17638, 2023.
- [27] Changkun Liu, Shuai Chen, Yukun Zhao, Huajian Huang, Victor Prisacariu, and Tristan Braud. Hr-apr: Apr-agnostic

- framework with uncertainty estimation and hierarchical refinement for camera relocalisation. In *2024 IEEE International Conference on Robotics and Automation (ICRA)*, pages 8544–8550. IEEE, 2024.
- [28] Changkun Liu, Shuai Chen, Yash Sanjay Bhalgat, Siyan HU, Ming Cheng, Zirui Wang, Victor Adrian Prisacariu, and Tristan Braud. Gs-cpr: Efficient camera pose refinement via 3d gaussian splatting. In *ICLR*, 2025.
- [29] Dominic Maggio, Marcus Abate, Jingnan Shi, Courtney Mario, and Luca Carlone. Loc-nerf: Monte carlo localization using neural radiance fields. In *2023 IEEE International Conference on Robotics and Automation (ICRA)*, pages 4018–4025, 2023.
- [30] Bortolon Matteo, Theodore Tsesmelis, Stuart James, Fabio Poiesi, and Alessio Del Bue. 6dgs: 6d pose estimation from a single image and a 3d gaussian splatting model. In *ECCV*, pages 420–436. Springer, 2024.
- [31] Arthur Moreau, Nathan Piasco, Dzmitry Tsishkou, Bogdan Stanculescu, and Arnaud de La Fortelle. Lens: Localization enhanced by nerf synthesis. In *Conference on Robot Learning*, pages 1347–1356. PMLR, 2022.
- [32] Arthur Moreau, Nathan Piasco, Moussab Bennehar, Dzmitry Tsishkou, Bogdan Stanculescu, and Arnaud de La Fortelle. Crossfire: Camera relocalization on self-supervised features from an implicit representation. In *ICCV*, pages 252–262, 2023.
- [33] Vojtech Panek, Zuzana Kukelova, and Torsten Sattler. Meshloc: Mesh-based visual localization. In *ECCV*, pages 589–609. Springer, 2022.
- [34] Paul-Edouard Sarlin, Cesar Cadena, Roland Siegwart, and Marcin Dymczyk. From coarse to fine: Robust hierarchical localization at large scale. In *CVPR*, pages 12716–12725, 2019.
- [35] Paul-Edouard Sarlin, Daniel DeTone, Tomasz Malisiewicz, and Andrew Rabinovich. Superglue: Learning feature matching with graph neural networks. In *CVPR*, pages 4938–4947, 2020.
- [36] Torsten Sattler, Bastian Leibe, and Leif Kobbelt. Efficient & effective prioritized matching for large-scale image-based localization. *IEEE TPAMI*, 39(9):1744–1756, 2016.
- [37] Torsten Sattler, Qunjie Zhou, Marc Pollefeys, and Laura Leal-Taixe. Understanding the limitations of cnn-based absolute camera pose regression. In *CVPR*, pages 3302–3312, 2019.
- [38] Yoli Shavit, Ron Ferens, and Yosi Keller. Learning multi-scene absolute pose regression with transformers. In *ICCV*, pages 2733–2742, 2021.
- [39] Jamie Shotton, Ben Glocker, Christopher Zach, Shahram Izadi, Antonio Criminisi, and Andrew Fitzgibbon. Scene coordinate regression forests for camera relocalization in rgb-d images. In *CVPR*, pages 2930–2937, 2013.
- [40] Linus Svärm, Olof Enqvist, Fredrik Kahl, and Magnus Oskarsson. City-scale localization for cameras with known vertical direction. *IEEE TPAMI*, 39(7):1455–1461, 2016.
- [41] Gabriele Trivigno, Carlo Masone, Barbara Caputo, and Torsten Sattler. The unreasonable effectiveness of pre-trained features for camera pose refinement. In *CVPR*, pages 12786–12798, 2024.
- [42] Julien Valentin, Angela Dai, Matthias Nießner, Pushmeet Kohli, Philip Torr, Shahram Izadi, and Cem Keskin. Learning to navigate the energy landscape. In *2016 Fourth International Conference on 3D Vision (3DV)*, pages 323–332. IEEE, 2016.
- [43] Fangjinhua Wang, Xudong Jiang, Silvano Galliani, Christoph Vogel, and Marc Pollefeys. Glace: Global local accelerated coordinate encoding. In *CVPR*, pages 21562–21571, 2024.
- [44] Jianyuan Wang, Minghao Chen, Nikita Karaev, Andrea Vedaldi, Christian Rupprecht, and David Novotny. Vggt: Visual geometry grounded transformer. In *CVPR*, pages 5294–5306, 2025.
- [45] Shuzhe Wang, Vincent Leroy, Yohann Cabon, Boris Chidlovskii, and Jerome Revaud. Dust3r: Geometric 3d vision made easy. In *CVPR*, pages 20697–20709, 2024.
- [46] Yifan Wang, Jianjun Zhou, Haoyi Zhu, Wenzheng Chang, Yang Zhou, Zizun Li, Junyi Chen, Jiangmiao Pang, Chunhua Shen, and Tong He. π^3 : Permutation-equivariant visual geometry learning. *arXiv preprint arXiv:2507.13347*, 2025.
- [47] Jianing Yang, Alexander Sax, Kevin J. Liang, Mikael Henaff, Hao Tang, Ang Cao, Joyce Chai, Franziska Meier, and Matt Feiszli. Fast3r: Towards 3d reconstruction of 1000+ images in one forward pass. In *CVPR*, pages 21924–21935, 2025.
- [48] Luwei Yang, Rakesh Shrestha, Wenbo Li, Shuaicheng Liu, Guofeng Zhang, Zhaopeng Cui, and Ping Tan. Scenescreeper: Learning to compress scene for camera relocalization. In *CVPR*, pages 8259–8268, 2022.
- [49] Lin Yen-Chen, Pete Florence, Jonathan T Barron, Alberto Rodriguez, Phillip Isola, and Tsung-Yi Lin. inerf: Inverting neural radiance fields for pose estimation. In *2021 IEEE/RSJ International Conference on Intelligent Robots and Systems (IROS)*, pages 1323–1330. IEEE, 2021.
- [50] Boming Zhao, Luwei Yang, Mao Mao, Hujun Bao, and Zhaopeng Cui. Pnerfloc: Visual localization with point-based neural radiance fields. In *AAAI*, pages 7450–7459, 2024.
- [51] Qunjie Zhou, Maxim Maximov, Or Litany, and Laura Leal-Taixé. The perfect match: Exploring nerf features for visual localization. In *ECCV*, pages 108–127. Springer, 2024.